CHEMISTRY OF MATERIALS

Open Access

pubs.acs.org/cm

Article

Probing the Aqueous Electrochemical Degradation in $Na_{2.5}V_{1.5}Ti_{0.5}(PO_4)_3$ by Nuclear Magnetic Resonance through the Interplay between Paramagnetic and Diamagnetic Vanadium Ions

Aurimas Dubauskas, Nadežda Traškina, Jurgis Pilipavičius, Linas Vilčiauskas,* and Vytautas Klimavicius*

Cite This: *Chem. Mater.* 2026, 38, 8829–8837

Read Online

ACCESS | Metrics & More | Article Recommendations | Supporting Information

ABSTRACT: Although nuclear magnetic resonance (NMR) spectroscopy is a very powerful method for investigating battery materials, its application is often complicated by the inherent presence of paramagnetic transition-metal ions (e.g., $V^{3+/4+}$, $Mn^{2+/3+}$, $Fe^{2+/3+}$, $Ni^{2+/3+}$, etc.). These ions induce extremely large chemical shift ranges, severe line broadening, and rapid spin relaxation, which often prevents NMR signal detection. In this work, we demonstrate that the interplay between the oxidation states and magnetic properties of vanadium, such as the transition from paramagnetic $V^{3+/4+}$ to diamagnetic V^{5+}, lead to the formation of local environments suitable for the NMR signal detection of multiple nuclei (e.g., ^{51}V, ^{31}P) which serve as unique and direct probes into the structure and degradation mechanism of vanadium-based battery materials. By systematically analyzing the NASICON-structured $Na_{2.5}V_{1.5}Ti_{0.5}(PO_4)_3$ samples, ranging from pristine NVTP powder to electrodes subjected to electrochemical cycling, we develop a comprehensive mechanistic model of NVTP electrochemical degradation in aqueous media. Our findings reveal that vanadium dissolution, together with phosphate, are among the primary drivers of charge capacity loss. The formation of residual Ti-containing phases, which also become NMR-visible due to the formation of diamagnetic V^{5+}, results in blocking layer growth and additional capacity loss. These NMR observations establish a definitive framework for probing the structure and stability of vanadium-based battery materials.

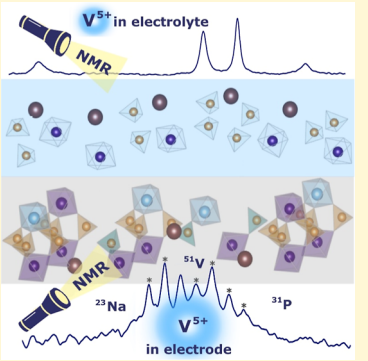

INTRODUCTION

Aqueous sodium-ion batteries based on noncritical materials, simple and inherently safe aqueous electrolytes, and novel electrochemical cell concepts represent a promising alternative for large-scale stationary energy storage.[1,2] However, their major limitation stems from the narrow electrochemical stability window of water, which constrains the selection of suitable electrode materials and lowers the achievable energy density. NAtrium SuperIonic CONductor (NASICON) structure type compounds have emerged as one of the most attractive classes of electrode materials for sodium-ion batteries. This is due to their compositional diversity, a wide range of accessible redox potentials, structural and thermal stability, high ionic conductivity, and charge capacity.[3−5] Nevertheless, limited aqueous stability, on both the negative and positive electrode sides, arising from metal dissolution, as well as the formation of blocking solid−electrolyte interphase layers, hinders their practical implementation in aqueous sodium-ion batteries.[6−9]

Vanadium-based $Na_3V_2(PO_4)_3$ (NVP) NASICON is an attractive and widely used positive electrode material owing to its high electrode potential (~3.4 V versus Na^+/Na), specific charge capacity (theoretically 117.6 mAh g^{-1}), ionic conductivity and thermal stability.[10−13] Although NVP performs well in organic and water-in-salt electrolytes, it suffers from rapid capacity degradation in low-concentration aqueous systems.[14,15] Both chemically and electrochemically induced dissolution of vanadium species from the electrode into the aqueous electrolyte is typically identified as a major contributor to capacity loss.[8,14] Nevertheless, the mechanism of vanadium dissolution remains unclear: is it driven by the aqueous thermodynamic stability of dissolved V^{5+} species or is it due to the lattice destabilization induced by bulk V^{5+} generation?

Several improvement strategies have been explored, including the development of tailored electrolytes and the use of surface coatings or dopants on active-material particles.[15−17] However, partial substitution of V with Ti in $Na_{3-x}V_{2-x}Ti_x(PO_4)_3$ stands out for significantly improved stability. For example, $Na_2VTi(PO_4)_3$ (NVTP) shows particularly stable performance during charge−discharge cycling even in low-concentration aqueous solutions.[18−23] A distinct feature of NVTP is its ability to operate as a

Received: April 3, 2026
Revised: August 11, 2026
Accepted: August 12, 2026
Published: August 21, 2026

bifunctional electrode, because the V^{3+}/V^{4+} and Ti^{3+}/Ti^{4+} redox couples can serve as positive and negative electrodes in aqueous systems, respectively.[23−25]

The stability of this system, on the positive side, is more important for practical applications. We have recently reported on $Na_{3-x}V_{2-x}Ti_x(PO_4)_3$ ($0.0 < x < 1.0$), showing solid-solution behavior across the complete V/Ti composition range and increasing stability in 1 M Na_2SO_4(aq) with higher Ti content.[9] For example, $Na_{2.25}V_{1.25}Ti_{0.75}(PO_4)_3$ composition is relatively stable in simple aqueous electrolyte solutions during electrochemical cycling at low C-rates.

Practical development of NASICON-based electrodes requires a detailed mechanistic understanding of the degradation processes that lead to capacity loss. Unfortunately, many widely used analytical techniques, such as X-ray diffraction (XRD), lack sufficient sensitivity, while Raman spectroscopy suffers from limited selectivity and challenging interpretation for detecting and identifying amorphous degradation products. Therefore, methods such as NMR spectroscopy can provide invaluable insights into processes occurring at the electrode−electrolyte interface during electrochemical operation.[26−29] Previous studies have successfully investigated a range of NASICON-based materials for battery applications, including $NaTi_2(PO_4)_3$, $Na_3V_2(PO_4)_2F_3$, $Na_{3+y}V_{2-y}Mg_y(PO_4)_3$, etc.[30−33] In addition, *ex situ* and *in situ* high-resolution liquid NMR was applied to investigate the evolution of electrolytes during electrochemical operation.[34−36]

Despite its importance and applicability in battery research, NMR spectroscopy faces substantial challenges because many electrode materials contain paramagnetic ions such as $V^{3+/4+}$, $Mn^{2+/3+}$, $Fe^{2+/3+}$, $Ni^{2+/3+}$, etc.[37] This results in rapid spin relaxation and severe line broadening, which often prevents NMR signal detection.[38] In addition, the Fermi contact interaction between unpaired electrons and the neighboring nuclei, as well as pseudocontact interactions in the case of further distanced nuclei, broaden the chemical shift range to several thousand ppm, rendering excitation and spectral acquisition particularly difficult.[32,39] Nevertheless, these experimental challenges can, in some cases, be mitigated by the intrinsic materials properties. For example, certain paramagnetic species such as V^{3+} or V^{4+} may be converted to diamagnetic species such as V^{5+} either because of normal electrochemical operation or as a result of degradation. The formation of V centers might provide a local diamagnetic environment where neighboring nuclei become NMR-detectable, enabling the observation of various properties and processes that would otherwise remain hidden.[40]

In this study, we combine *ex situ* multinuclear ^{23}Na, ^{13}C, ^{31}P, and ^{51}V solid-state NMR, and powder X-ray diffractometry (XRD) of the electrodes, as well as ^{31}P, ^{51}V high-resolution NMR of the liquid electrolytes to investigate the aqueous electrochemical degradation of $Na_{2.5}V_{1.5}Ti_{0.5}(PO_4)_3$ electrodes. This composition was selected as a compromise between its vanadium content and aqueous stability, allowing us to remain on the V-rich side while still observing substantial capacity fade during charge−discharge cycling, which is necessary for observing the degradation processes and detecting their products.

EXPERIMENTAL SECTION

Material Synthesis

$Na_{2.5}V_{1.5}Ti_{0.5}(PO_4)_3$−carbon composite was synthesized by the aqueous sol−gel method. 10 mmol of citric acid ($C_6H_8O_7$, p.a., Lach-Ner) was dissolved in 500 mL of deionized water. 12.5 mmol of sodium carbonate (Na_2CO_3, ≥99.9%, Fischer Chemicals), 30 mmol of ammonium dihydrogen phosphate ($NH_4H_2PO_4$, >99%, Honeywell), and 15 mmol of ammonium metavanadate (NH_4VO_3, ≥99%, Roth) were added to the solution to react under continuous stirring. Subsequently, 5 mmol of titanium isopropoxide ($Ti(OC_4H_9)_4$, ≥98%, Acros Organics) was added to isopropanol (20 mL) to prevent contact with moisture, and the mixture was agitated. Then, it was immediately added to a precursor solution, which was stirred at 60 °C overnight to complete the reaction. Water and isopropanol were evaporated on a hot plate. The resulting powder was ground and calcined at 350 °C for 5 h, then reground and calcined at 800 °C for 12 h in a tube furnace under a flowing N_2 atmosphere. The obtained particles were reground and additionally ball-milled (Retsch, PM 400) for 1 h at 450 rpm in isopropanol, followed by drying at 70 °C.

Electrode Preparation

The electrode slurry was prepared by mixing 70 wt % of $Na_{2.5}V_{1.5}Ti_{0.5}(PO_4)_3$−C, 20 wt % of carbon black (Super-P, TIMCAL), and 10 wt % of polyvinylidene fluoride (PVDF, $(C_2H_2F_2)_n$, HSV1800, Kynar) in *N*-methyl-2-pyrrolidone (C_5H_9NO, Sigma-Aldrich, 99.5%). Dry components were premixed in a planetary ball mill (Retsch, PM 400) for 1 h at 175 rpm. Then, the slurry was homogenized for 2 h at 350 rpm and subsequently cast into a film. After drying in a vacuum for 3 h at 120 °C, the resulting electrode film was punch-cut into 32 mm diameter disks and transferred onto 316L stainless steel mesh (#325) by pressing in the calendaring machine (Tob New Energy, TOB-DG-100L). For the electrodes prepared for quantitative XRD analysis, the slurry composition was modified by adding monoclinic ZrO_2 (Alfa Aesar, 99%) as an inert internal standard, using an NVTP/ZrO_2/carbon black/PVDF mass ratio of 6/1/2/1, corresponding to 60/10/20/10 wt %.

Electrochemical Characterization

The electrochemical characterization of NVTP was performed in decoupled three-electrode beaker-type half-cells under flooded electrolyte conditions in naturally aerated 1 M Na_2SO_4(aq) solutions to facilitate active material degradation. In this setup, the working NVTP electrode and the copper rod counter electrodes were placed in separate compartments connected by a 1 M $NaNO_3$ (in-agarose) salt bridge. The working NVTP electrode was placed in 30 mL of 1 M Na_2SO_4(aq) electrolyte. $Hg/Hg_2SO_4/K_2SO_4$ (aq sat) (MSE) or Ag/AgCl/KCl (aq sat) were used as a reference electrode. Galvanostatic charge−discharge (GCD) cycling was carried out on a battery tester (Neware CT-4008) in the range from −0.25 V to 0.25 V vs MSE or 0.2 V to 0.7 V vs Ag/AgCl at 27 mA g^{-1}.

For further characterization, the electrodes and electrolyte solutions were collected after a predefined number of GCD cycles. Electrodes were carefully rinsed with deionized water to remove Na_2SO_4, stripped off the mesh in the sonication bath, dried, and ground into powder. For the *in situ*/*operando* pH monitoring, a pH meter (Mettler Toledo SevenCompact S220) equipped with a combination pH probe (Mettler Toledo InLab Micro Pro-ISM) was used.

Powder X-ray Diffractometry

All X-ray diffraction measurements were performed on a Rigaku MiniFlex XpC X-ray diffractometer. Bragg−Brentano geometry, 0.02° step size, and 5°/min scan rate were used. Quantitative XRD analysis was performed by the Rietveld refinement method using ZrO_2 powder inert internal standard incorporated into the XRD-specific electrode formulation during slurry preparation. The GSAS II software suite was used for all Rietveld refinements.[41] The line shape parameters of the diffractometer were determined by recording and refining LaB_6 (NIST SRM 660c) standard XRD pattern. All NVTP/ZrO_2 electrode XRD pattern refinements were performed in batch mode using

https://doi.org/10.1021/acs.chemmater.6c00991
Chem. Mater. 2026, 38, 8829−8837

identical refinement settings. The monoclinic ZrO_2 lattice parameters were fixed as an internal reference, whereas the NVTP lattice parameters were refined independently for each electrode pattern.

NMR Characterization

All NMR experiments were carried out at 14.1 T on a Bruker Avance Neo 600 NMR spectrometer operating at 600.3, 243.7, 158.8, 151.0, 157,8 MHz for ^{1}H, ^{31}P, ^{23}Na, ^{13}C, ^{51}V, respectively. For *ex situ* high-resolution NMR measurements, a 5 mm Bruker $^{1}H-^{13}C$-BB TBI probe was used. A capillary insert containing a D_2O solution was used for the lock signal. For estimating the concentration of dissolved ions, quantitative ^{31}P and ^{51}V NMR measurements were performed at 298 K temperature using the following parameters: (a) for ^{31}P 25 μs $\pi/2$ excitation, 15 s recycle delay, and 2048 scans; (b) for ^{51}V 31.5 μs $\pi/2$ excitation, 5 s recycle delay, and 4096 scans. For ^{31}P NMR signal intensity calibration measurements, 0.0556 mol·L^{-1} $NH_4H_2PO_4$(aq) (ADP) in aqueous solution with 0.1 mol·L^{-1} Na_2SO_4(aq) was used. For ^{51}V NMR signal intensity calibration measurements, 0.0556 mol·L^{-1} NH_4VO_3(aq) with 0.1 mol·L^{-1} Na_2SO_4(aq) was used.

For *ex situ* solid-state NMR measurements, a Bruker 2.5 mm trigamma triple-resonance MAS probe was used. Samples were packed in 2.5 mm zirconia rotors, and 10−30 kHz MAS was used. The temperature was stabilized at 298 K. For ^{31}P measurements, a saturation recovery pulse sequence was employed, consisting of a saturation pulse train of 20 $\pi/2$ pulses, followed by a 1 s delay and $\pi/2$ pulse. For some ^{31}P measurements Hahn-echo pulse sequence ($\pi/2-$delay$-\pi-$acquire) using one rotor period as echo delay was used. The $\pi/2$ excitation pulse was equal to 3.57 μs, and 256−147,456 scans were accumulated. For ^{23}Na measurements, single-pulse excitation was used and 2048−40,960 scans were accumulated depending on the relaxation delay (0.1−0.05 s). For ^{51}V measurements, the Hahn-echo pulse sequence using 2 rotor periods as the echo delay was used and $\pi/2$ pulse was set to 2.9 μs. For ^{13}C measurements, direct excitation was used; a $\pi/2$ excitation pulse of 4.84 μs with spinal 64 decoupling was used. ^{31}P, ^{23}Na, ^{51}V, ^{13}C MAS NMR spectra were referenced using ammonium dihydrogen phosphate ($NH_4H_2PO_4$, $\delta(^{31}P)$ = 0.8 ppm), sodium chloride (NaCl, $\delta(^{23}Na)$ = 0 ppm), vanadium(V) oxide (V_2O_5 $\delta(^{51}V)$ = −611 ppm) and adamantane ($C_{10}H_{16}$, $\delta(^{13}C)$ = 39.0 and 29.9 ppm) as external standards.

RESULTS AND DISCUSSION

Electrochemical Properties

The electrochemical characterization of NVTP electrodes was performed over the potential range in which only the V^{3+}/V^{4+} redox pair is active. In this case, the sodium ion insertion reaction could be expressed as

$$2Na_{2.5}V^{3+}_{1.5}Ti^{4+}_{0.5}(PO_4)_3 \leftrightarrow 2NaV^{4+}_{1.5}Ti^{4+}_{0.5}(PO_4)_3 + 3e^- + 3Na^+ \quad (1)$$

The specific capacity during GCD cycling is shown in Figure 1. The results show rapid capacity loss in the early cycles, with *ca.* 50% of the initial discharge capacity lost during the first 15−20 cycles. Typically, this capacity loss is attributed to vanadium dissolution into the electrolyte.[9] Most of the vanadium dissolves into the electrolyte during charging, ending up in the V^{5+} state, while lower pH conditions further accelerate degradation by promoting both chemical dissolution and electrochemically induced formation of soluble V^{4+}.[8] Consistent with previous reports, the 1 M Na_2SO_4(aq) electrolyte gradually changed from transparent to a yellow-green color during GCD cycling, typical of VO_2^+(aq) species.[9]

In this work, we also perform *in situ/operando* pH monitoring during GCD cycling using a pH microelectrode. The pH microelectrode tip was placed as close as possible (*ca.* 1 mm) to the working electrode surface, enabling the

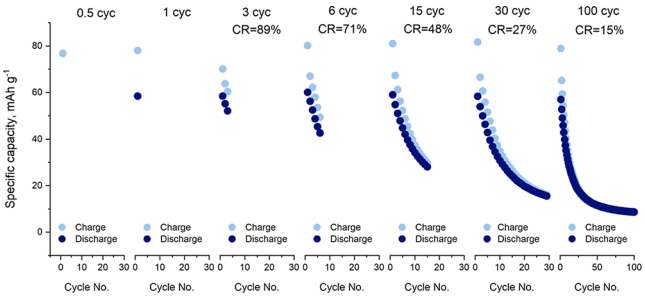

Figure 1. GCD cycling performance and capacity retention (CR) of NVTP electrodes in naturally aerated 1 M Na_2SO_4(aq) at 27 mA g^{-1} specific current after 0.5, 1, 3, 6, 15, 30, and 100 cycles.

observation of localized pH changes at the electrode surface. The data presented in Figure 2a show a slight but continuous decrease in electrolyte pH during the 6 h resting period prior to cycling. This behavior indicates that chemical degradation of

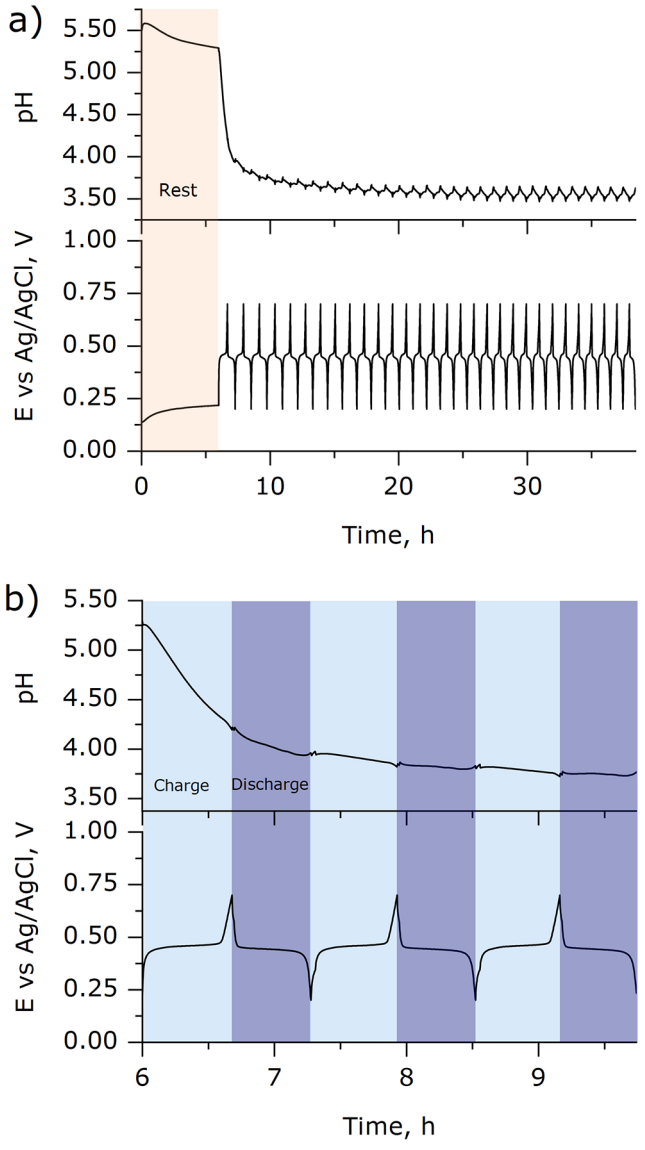

Figure 2. Local electrolyte pH and charge−discharge potential profiles of NVTP electrodes during GCD cycling: (a) 1−30 GCD cycles; (b) 1−3 GCD cycles.

https://doi.org/10.1021/acs.chemmater.6c00991
Chem. Mater. 2026, 38, 8829−8837

NVTP already starts upon contact with the aqueous electrolyte. Consistent with this interpretation, high-resolution liquid-state NMR measurements detect dissolved vanadium species in the electrolyte even before the first GCD cycle, while the control experiment containing only carbonaceous electrode components shows no measurable pH change (Figure S3 in Supporting Information). These observations suggest that the initial acidification originates from chemical dissolution and aqueous speciation of vanadium species released from the NVTP. It then reacts with oxygen present in naturally aerated aqueous electrolyte to form pervanadyl species according to the Pourbaix diagram[42]

$$3V^{5+} + O_2 + 4H_2O \rightarrow 3VO_2^+ + 8H^+ \quad (2)$$

During the first charging step, the pH drops from *ca.* 5.5 to *ca.* 4, indicating significant generation of V^{5+} species in the electrolyte. The sudden drop in pH might also produce some electrochemically induced soluble V^{4+} species during cycling, which further accelerates material degradation and pH rise, as shown in our previous study[8]

$$2V^{4+} + \frac{1}{2}O_2 + 3H_2O \rightarrow 2VO_2^+ + 6H^+ \quad (3)$$

The pH stabilizes at ~3.6 after ~15 charge−discharge cycles and then fluctuates only slightly during the remaining GCD cycling.

To evaluate how active material dissolution contributes to capacity loss, the NVTP phase content was monitored by powder XRD at various stages of electrochemical cycling *ex situ* (Figure 5). Quantitative analysis of the NVTP fraction was performed using the Rietveld refinement and ZrO_2 powder as an inert internal standard. As summarized in Figure 5b, the NVTP phase content in the electrode correlates to the capacity loss during early GCD cycles. This indicates that NVTP charge capacity fade is mainly driven by the loss of active material. Only in the later cycles does a noticeable deviation from linearity appear. This is a result of some additional processes, such as the formation of blocking interphasial layers, which lead to contact loss for the active material particles, similarly to what was observed for $NaTi_2(PO_4)_3$.[7]

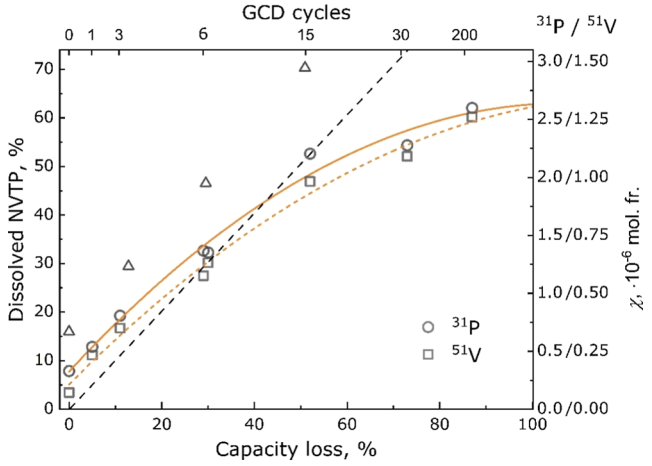

Figure 3. Evolution of phosphorus (circles) and vanadium (squares) molar fractions in the electrolyte derived from the integral intensities of the ^{31}P and ^{51}V NMR signals, alongside the calculated fraction of dissolved NVTP from the electrode as a function of capacity loss during cycling. Orange lines are second-order polynomial fits of ^{31}P (solid) and ^{51}V (dashed) data, and the gray dashed line shows the linear dependency for comparison. The triangles show the NVTP phase-loss obtained from XRD analysis for comparison. Note that the concentration values are normalized to 1 mg of NVTP material.

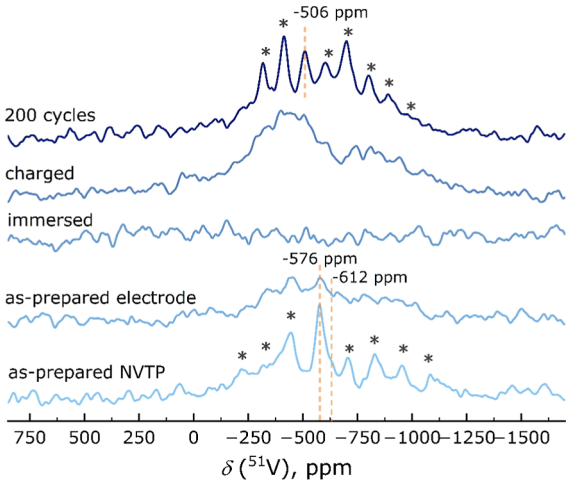

Figure 4. *Ex situ* ^{51}V MAS NMR spectra of as-prepared powder, as-prepared, and cycled NVTP electrodes. MAS spinning sidebands are indicated by asterisks.

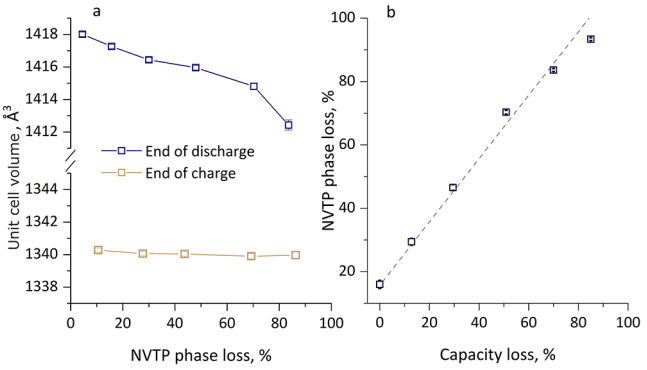

Figure 5. (a) Refined NVTP unit cell volume as a function of NVTP phase loss during GCD cycling. The data are shown for electrodes at the end of charging (0.7 V vs Ag/AgCl) and at the end of discharging (0.2 V vs Ag/AgCl). The lattice volume in the charged state remains nearly constant, whereas in the discharged state progressively decreases with increasing NVTP phase loss. (b) NVTP phase loss fraction as obtained by XRD versus discharge capacity lost during GCD cycling.

Ex Situ High-Resolution Liquid NMR Investigation of the Electrolytes

To quantitatively analyze the degradation process, *ex situ* high-resolution ^{31}P and ^{51}V NMR measurements were performed on the collected electrolyte samples at different stages of GCD cycling. ^{31}P and ^{51}V NMR spectra are excellent probes for quantitatively characterizing dissolution processes, which, unlike, e.g., ^{23}Na NMR, do not interfere with the electrolyte solution itself. In the high-resolution ^{31}P NMR spectrum of the electrolyte after the electrode immersion but prior to GCD cycling, a weak resonance at 0.5 ppm is observed (Figure S4 in Supporting Information). However, once GCD cycling starts, a signal appears at −0.05 ppm, and its intensity increases with the number of cycles, as shown in Figure S4 in Supporting Information. The observed ^{31}P chemical shift indicates the

https://doi.org/10.1021/acs.chemmater.6c00991
Chem. Mater. 2026, 38, 8829−8837

formation of aqueous HPO_4^{2-} ions, resulting from electrochemically induced degradation of NVTP.

In the high-resolution ^{51}V NMR spectrum of the electrolyte after the electrode immersion but prior to GCD cycling, a resonance at −558 ppm is observed (Figure S5 in Supporting Information). The ^{51}V chemical shift indicates that vanadium species in the electrolyte are in the V^{5+} oxidation state. At the beginning of the GCD cycling, a series of resonances at −422, −502, and −520 ppm becomes visible. These ^{51}V NMR lines could be assigned to aqueous decavanadate $[V_{10}O_{28}]^{6-}$ species.[43] It should be noted that all ^{51}V signals at −558, −520, −502, −422 ppm are integrated and used in further quantitative analysis.

Figure 3 presents the evolution of phosphorus and vanadium molar fractions derived from the integral intensities of the ^{31}P and ^{51}V NMR signals, alongside the calculated fraction of dissolved NVTP from the electrode as a function of capacity loss during cycling. The concentrations of phosphorus and vanadium increase linearly with capacity loss during the initial cycles. A deviation from linearity is observed beyond *ca.* 50% capacity loss, where the concentrations of leached species start to level off. These results suggest that while active material dissolution dominates the initial capacity fade, the degradation mechanism in later cycles shifts toward the loss of electrical contact between the NVTP and the conductive carbon particles, as also confirmed by the quantitative XRD phase analysis. The V/P molar ratio of approximately 2 in the electrolyte remains stable throughout cycling. This suggests that vanadium and phosphate species dissolve at the same rate from the $Na_{2.5}V_{1.5}Ti_{0.5}(PO_4)_3$ framework, leading to structural degradation and capacity loss.

Ex Situ Solid-State NMR and XRD Investigation of the Electrodes

To gain deeper insight into NVTP electrode degradation mechanisms, we first perform ^{51}V MAS NMR measurements on the pure NVTP powder and as-prepared electrodes, followed by *ex situ* analysis of electrodes removed from the cell after a predefined number of full- or half-GCD cycles (Figures 4, S6, and S7 in Supporting Information). In the case of NVTP powder, highly overlapped lines are observed at −576 and −612 ppm (Figure 4). We suggest that this signal originates from the surface residual oxidic and phosphatic V^{5+} species.[30,44,45] Due to quadrupolar interaction (^{51}V $I = 7/2$) and paramagnetic nature of the material, the observed line widths are broad, preventing further rigorous spectral analysis. The as-prepared composite NVTP electrode exhibits the same ^{51}V NMR signals as those of pure NVTP powder. Prior to GCD cycling, vanadium in the NVTP electrodes primarily exists in the V^{3+} oxidation state, with a potentially small amount of V^{4+}. Because both species are paramagnetic and NMR-silent, only V^{5+} is detectable. However, the subsequent disappearance of the ^{51}V signals in MAS NMR upon immersion of the electrode in the electrolyte indicates the near-complete dissolution of surface V^{5+} species.

During GCD cycling, a resonance at −506 ppm begins to emerge in the ^{51}V MAS NMR spectra (Figures 4 and S7 in Supporting Information). The appearance of this signal indicates the formation of V^{5+} species that are no longer dissolved into the electrolyte but are retained within the electrode. As readily soluble V^{5+} species should dissolve during cycling and electrode washing, the persistence of this ^{51}V NMR signal suggests the presence of locally confined V^{5+} environments within the NVTP framework. The approximately 70 ppm difference from the surface V^{5+} NMR signal observed in the pristine powder further supports the hypothesis that these species occupy a distinct local environment.

The ^{51}V MAS NMR data assignment is consistent with the *ex situ* XRD results. Rietveld refinement reveals a distinct asymmetry in the evolution of the NVTP lattice volume during GCD cycling (Figure 5a). While the lattice volume of charged (electrochemically oxidized) NVTP remains constant at approximately 1340 Å^3, the lattice volume of discharged (electrochemically reduced) NVTP shows a slight decrease from 1417 to 1412 Å^3 as the NVTP phase loss reaches ∼80% during GCD cycling. It should be noted that quantitative phase analysis was possible down to approximately 6% of the remaining crystalline NVTP, whereas reliable extraction of lattice parameters was not possible beyond ∼80% phase loss due to very low NVTP diffraction intensity. These results could be explained by assuming that NVTP lattice volume only depends on the degree of sodiation and the continuous accumulation of a small fraction of V^{5+} δ in the form of V/Na antisite defects in the NASICON structure, which could be expressed as

$$\begin{aligned} &Na_{2.5}V^{3+}_{1.5}Ti_{0.5}(PO_4)_3 \\ &\xrightarrow{\text{charge}} (Na_{1-\delta}V^{5+}_{\delta})V^{4+}_{1.5-\delta}Ti_{0.5}(PO_4)_3 + (1.5+\delta)e^- \\ &\quad + (1.5+\delta)Na^+ \\ &\xrightarrow{\text{discharge}} (Na_{1-\delta}V^{5+}_{\delta})V^{4+}_{1.5-\delta}Ti_{0.5}(PO_4)_3 + (1.5+\delta)e^- \\ &\quad + (1.5+\delta)Na^+ \\ &\quad (Na_{2.5-2\delta}V^{5+}_{\delta})V^{3+}_{1.5-\delta}Ti_{0.5}(PO_4)_3 + (1.5-\delta) \\ &\quad e^- + (1.5-\delta)Na^+ \end{aligned} \tag{4}$$

This scenario is supported by our NMR results and has been previously reported in various NASICON compounds.[46,47] During the charging step, the electrochemically active vanadium is oxidized from V^{3+} to V^{4+}, and sodium ions in the NASICON M2 sites are extracted from the NVTP structure. This leads to only the M1 sites being occupied by sodium, which cannot be further extracted under these conditions. This is a reason why the NVTP lattice parameters in the charged state remain independent of the degree of NVTP degradation. However, a significant fraction of vanadium migrates away from its usual site in the NVTP structure and is oxidized to V^{5+} and dissolved into the electrolyte. During the subsequent discharge step, V^{5+} can further migrate within the NASICON structure forming a small concentration δ of Na/V^{5+} antisite defects in the NVTP framework (eq 4). The accumulation of such defects does not change the NVTP lattice constant in the desodiated charged state but reduces the amount of redox-active vanadium at the typical site in the NASICON structure and the sodiation capacity of NVTP during charging due to charge neutrality. This leads to a constant decrease in the NVTP lattice constant in the discharged (sodiated) state during GCD cycling and degradation of this material in aqueous environments. The formation and accumulation of such antisite V^{5+}/Na defects also well corroborates the NMR results.

To gain deeper insight into NVTP electrode degradation mechanisms, ^{31}P MAS NMR measurements on the pristine NVTP powder and as-prepared electrodes, followed by *ex situ*

https://doi.org/10.1021/acs.chemmater.6c00991
Chem. Mater. 2026, 38, 8829−8837

analysis of electrodes removed from the cell after a predefined number of GCD cycles were performed. The ^{31}P MAS NMR spectrum of the pristine active NVTP material shows three signals at 5900, 3000, and 3 ppm (Figure S8 in Supporting Information). The ^{31}P NMR signals at 5900 and 3000 ppm are attributed to NVTP phosphorus species near V^{3+}. These ^{31}P nuclei experience strong Fermi contact interaction with the unpaired electrons of the paramagnetic V^{3+} centers, leading to high chemical shift values. Similar signals in the 6100−1600 ppm range have previously been reported for NVP and NVPF materials.[31,32,48] We attribute the ^{31}P NMR signal at 3 ppm to species located at or near the particle surface. Such a chemical shift is due to surface vanadium species that are in the oxidation state V^{5+}, which predetermines diamagnetic ^{31}P chemical environment. The ^{31}P MAS NMR spectrum of the freshly prepared NTVP electrode retains the same characteristic resonances, though with reduced signal intensity (Figures 6a and S8 in Supporting Information).

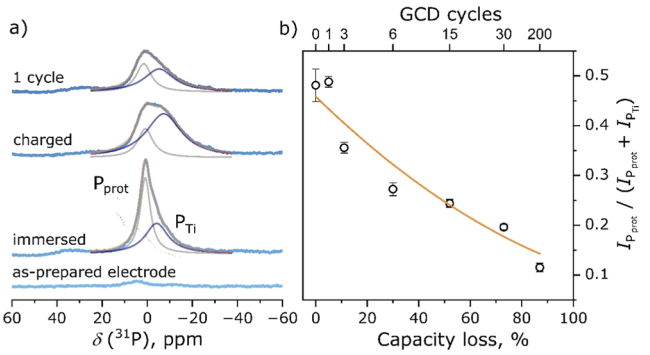

Figure 6. (a)*Ex situ* ^{31}P MAS NMR spectra obtained for as-prepared, immersed, and cycled NVTP electrodes; (b) the evolution of the $I_{Pprot}/(I_{Pprot} + I_{P_{Ti}})$ ratio during GCD cycling. The orange line represents a second-order polynomial fit.

After immersion of the NTVP electrode in the electrolyte for 10 h, the signals at 5900 and 3000 ppm remain (Figure S8 in Supporting Information), whereas the 3 ppm resonance disappears and two signals appear at 0.8 and −6 ppm (Figure 6a). We attribute the disappearance of the 3 ppm signal in the ^{31}P MAS NMR spectra during the initial immersion in electrolyte to the dissolution of surface phosphate species, consistent with the discussion in the previous section. During GCD cycling, the ^{31}P MAS NMR spectra show further changes: the signal at 0.8 ppm decreases in intensity, while the signal at −6 ppm remains constant. We attribute these signals to surface or near-surface defect sites that originated due to vanadium dissolution. The signal at 0.8 ppm is attributed to protonated surface phosphate groups that, after electrode removal and drying, are no longer in contact with paramagnetic V^{3+}/V^{4+} species.[49] The signal at −6 ppm corresponds to a phosphorus defect site, which is coordinated only by Ti-based units (Figure 9). This defect is probably incorporated within the NASICON framework close to the surface and resembles previously reported $TiO(OH)(H_2PO_4)\cdot nH_2O$ ($\delta(^{31}P)$ = −7 ppm) chemical environment.[33,50,51] Phosphates surrounded by Ti-based units are more stable in aqueous medium because of higher titanium sublattice stability, therefore the signal at −6 ppm remains constant. Based on the ^{51}V solid-state NMR data, the emergence of a ^{31}P NMR signal from phosphorus species coordinated with V^{5+} upon

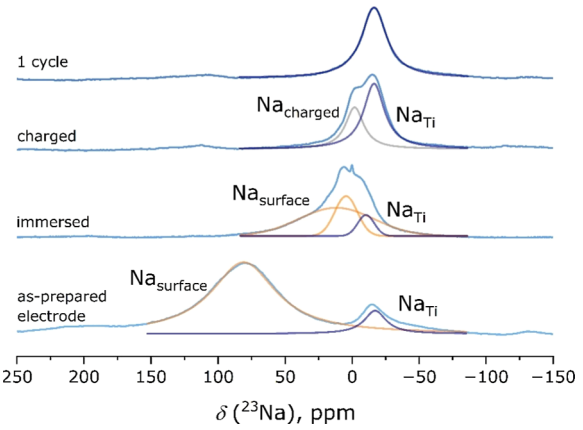

Figure 7. *Ex situ* ^{23}Na MAS NMR spectra obtained for as-prepared and cycled NVTP electrodes.

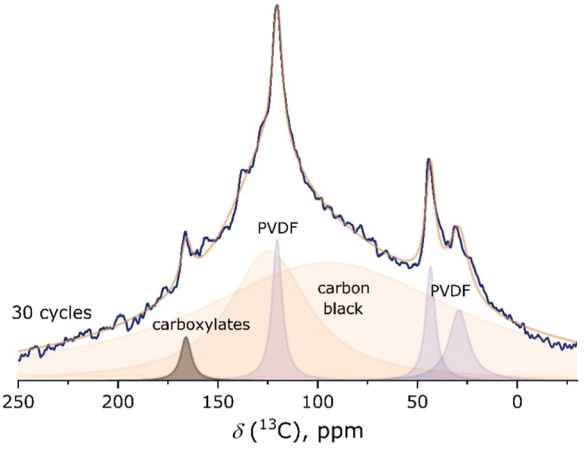

Figure 8. *Ex situ* ^{13}C MAS NMR spectra of NVTP electrodes after 30 GCD cycles.

GCD cycling is expected. Such a signal is not resolved in our data, most probably due to the overlap with a much stronger signal at −6 ppm, as the expected chemical shift value should be similar, and the amount of such species is rather low.[52] The evolution of phosphorus species during GCD cycling is estimated by calculating the ratio $I_{Pprot}/(I_{Pprot} + I_{PTi})$, where I_{Pprot} and I_{PTi} are the integral intensities of the signals assigned to the protonated surface phosphates free of surrounding paramagnetic V^{3+}/V^{4+} species, and phosphates fully surrounded by Ti-based units, respectively (Figure 6b). The decrease in this ratio during GCD cycling suggests that phosphate species coordinated to Ti-based units are more stable against dissolution and are preferentially retained at the NVTP electrode surface.

The ^{23}Na MAS NMR data for the pristine NVTP powder, as well as the as-prepared and cycled NVTP electrodes *ex situ*, are presented in Figures 7 and S9 in Supporting Information. The ^{23}Na MAS NMR spectrum of the pristine NVTP powder exhibits two signals at 80 ppm and −16 ppm, assigned to surface sodium species near diamagnetic V^{5+} and NASICON defects or sites where sodium is most probably statistically coordinated within Ti-based octahedra, respectively. The obtained chemical shift value of δ_{iso} = −16 ppm is very similar to that previously obtained for the NASICON-structured $NaTi_2(PO_4)_3$ (δ_{iso} = −14.5 ppm).[33] The as-prepared NVTP electrode retains the same spectral features. However,

https://doi.org/10.1021/acs.chemmater.6c00991
Chem. Mater. 2026, 38, 8829−8837

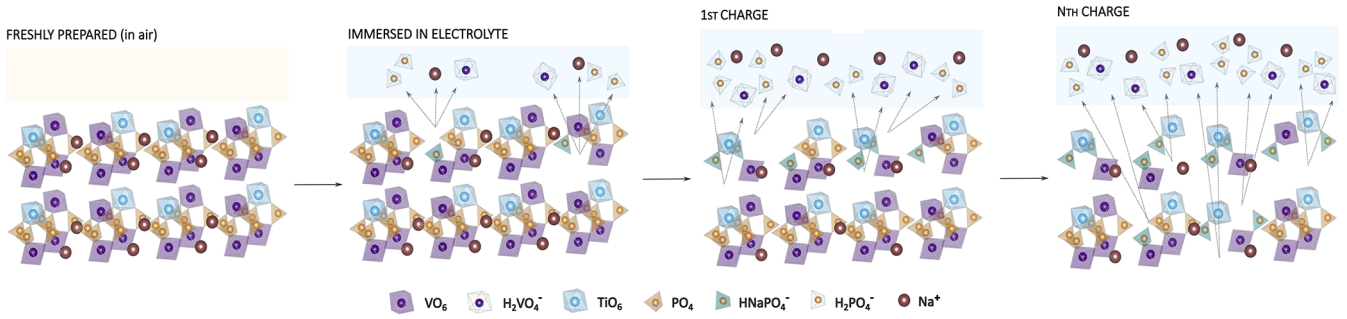

Figure 9. Schematic illustration of the dissolution mechanism of surface vanadium and phosphate species from the NVTP electrode into the aqueous electrolyte during initial immersion as well as GCD cycling.

significant spectral changes occur upon contact of the electrode with the electrolyte. While the resonance at −16 ppm remains, the signal at 80 ppm disappears, and peaks emerge at 12 and 4 ppm. The surface sodium ions associated with V^{5+} species dissolve in the aqueous electrolyte, which explains the disappearance of the ^{23}Na NMR signal at 80 ppm. The appearance of the ^{23}Na NMR signals centered at 12 and 4 ppm is attributed to several residual sodium species that remain attached after the electrode is removed from the electrolyte and dried. The large line width suggests the amorphous nature of these species. During the initial charge of the NVTP electrode, loosely bound surface phosphate species dissolve into the electrolyte, resulting in the permanent disappearance of the ^{23}Na NMR signal associated with these sodium atoms (Figure S9 in Supporting Information). In a charged electrode state, a ^{23}Na NMR signal at −2 ppm appears while a signal at −16 ppm remains in both the charged and discharged states throughout the GCD cycling range (Figures 7 and S9 in Supporting Information). The signal at −2 ppm is a clear marker of a charged electrode state. Its nature is most probably related to the formation of V^{5+}/Na antisite defects in the NVTP framework.

Finally, *ex situ* ^{13}C MAS NMR spectra were recorded for both the as-prepared and cycled composite electrodes (Figures 8 and S10 in Supporting Information). Unlike other spectra, the ^{13}C MAS NMR signals are attributed exclusively to the conductive fillers and the PVDF binder within the electrode matrix, rather than the NVTP active material. All studied ^{13}C MAS NMR spectra display multiple overlapping ^{13}C NMR signals between 0 and 150 ppm. The resolved peaks at 120, 44, and 31 ppm correspond to the PVDF binder, while the broad unresolved features at 124 and 95 ppm are attributed to the conductive carbon black filler.[53,54] A signal at 166 ppm appears after cycling, attributed to the formation of surface carboxylates on the carbonaceous phase (Figure 8). As reported in our previous study on $NaTi_2(PO_4)_3$, the development of such species is associated with parasitic reactions that might also contribute to capacity loss.[55,33] The ^{23}Na MAS NMR signal associated with such surface carboxylates is probably not resolved in this work due to significant overlap with other resonances (Figure 7).

CONCLUSIONS

In this study, we used multinuclear ^{13}C, ^{23}Na, ^{31}P, and ^{51}V *ex situ* solid-state NMR and high-resolution liquid NMR spectroscopy together with quantitative *ex situ* XRD analysis to investigate the aqueous electrochemical degradation of $Na_{2.5}V_{1.5}Ti_{0.5}(PO_4)_3$ electrodes. By systematically analyzing the results of NVTP samples, ranging from pristine NVTP powder and as-prepared electrodes to electrodes subjected to cycling, we have constructed a comprehensive mechanistic model of NVTP degradation and its associated capacity loss. This model captures the distinct stages of NVTP operation in aqueous environments. The NMR results revealed an interesting interplay between the various oxidation states and magnetic properties of vanadium in the NVTP. While the bulk of the active material is mostly composed of paramagnetic V^{3+} and V^{4+} in the discharged and charged states, respectively, NMR signals from these and surrounding phosphorus and sodium nuclei are significantly shifted to high chemical shift values or remain completely NMR-silent. However, the appearance of diamagnetic V^{5+} species provides a unique direct NMR probe into the structure and dynamics of vanadium-based materials. The formation of V^{5+} is associated with the surface oxidation and subsequent degradation of NVTP in aqueous electrolytes, starting with the immersion in the electrolyte solution and during its electrochemical operation. In addition, the formation of a small concentration of Na/V^{5+} antisite defects in the NVTP framework was detected. This, along with the formation of Ti-rich interphasial layers, provides a diamagnetic environment that facilitates the detection of ^{23}Na and ^{31}P NMR signals that would otherwise remain invisible or significantly shifted in NMR spectra. ^{31}P and ^{51}V high-resolution liquid NMR together with quantitative *ex situ* XRD analysis confirm that vanadium and phosphate species dissolve at the same rate from the electrode active material, leading to metal leaching, structural degradation, and associated capacity loss. The observed capacity loss in the initial cycles correlates linearly with P and V dissolution. However, beyond 50% capacity loss, this trend plateaus, indicating that later-stage degradation is driven by a loss of electrical contact between the NVTP and the conductive carbon particles. These results provide valuable insights into key degradation processes and products, allowing us to elucidate critical details of the NVTP degradation mechanism at different stages of its electrochemical operation. This understanding is essential for further development and practical application of this and related polyanionic systems in electrochemical devices.

ASSOCIATED CONTENT

Supporting Information

The Supporting Information is available free of charge at https://pubs.acs.org/doi/10.1021/acs.chemmater.6c00991.

Additional experimental data (PDF)

https://doi.org/10.1021/acs.chemmater.6c00991
Chem. Mater. 2026, 38, 8829−8837

AUTHOR INFORMATION

Corresponding Authors

Linas Vilčiauskas − *Center for Physical Sciences and Technology (FTMC), LT-10257 Vilnius, Lithuania; Institute of Chemistry, Vilnius University, LT-10257 Vilnius, Lithuania*; Email: linas.vilciauskas@ftmc.lt

Vytautas Klimavicius − *Institute of Chemical Physics, Vilnius University, LT-10257 Vilnius, Lithuania*; orcid.org/0000-0002-4549-1953; Email: vytautas.klimavicius@ff.vu.lt

Authors

Aurimas Dubauskas − *Institute of Chemical Physics, Vilnius University, LT-10257 Vilnius, Lithuania*; orcid.org/0009-0009-4398-9377

Nadežda Traškina − *Center for Physical Sciences and Technology (FTMC), LT-10257 Vilnius, Lithuania*; orcid.org/0009-0008-8853-3368

Jurgis Pilipavičius − *Center for Physical Sciences and Technology (FTMC), LT-10257 Vilnius, Lithuania; Institute of Chemistry, Vilnius University, LT-10257 Vilnius, Lithuania*

Complete contact information is available at: https://pubs.acs.org/10.1021/acs.chemmater.6c00991

Author Contributions

A.D.—Methodology, Investigation, Formal analysis, Data curation, Visualization, Validation, Writing-original draft. **N.T.**—Methodology, Investigation, Formal analysis, Data curation, Visualization, Validation, Writing-original draft. **J.P.**—Conceptualization, Methodology, Investigation, Supervision, Formal analysis, Data curation, Visualization, Validation, Writing-original draft. **L.V.**—Resources, Conceptualization, Methodology, Supervision, Investigation, Formal analysis, Data curation, Visualization, Validation, Writing-original draft, Writing-review and editing. **V.K.**—Funding acquisition, Project administration, Resources, Conceptualization, Methodology, Supervision, Investigation, Formal analysis, Data curation, Visualization, Validation, Writing-original draft, Writing-review and editing. The manuscript was written through the contributions of all authors. All authors have approved the final version of the manuscript.

Notes

The authors declare no competing financial interest.

ACKNOWLEDGMENTS

This project has received funding under the grant agreement with the Research Council of Lithuania (LMTLT) (Project No. S-MIP-23-47). V.K., A.D. acknowledge the Center of Spectroscopic Characterization of Materials and Electronic/Molecular Processes (SPECTROVERSUM Infrastructure) for the use of NMR spectrometer.

REFERENCES

(1) Chao, D.; Zhou, W.; Xie, F.; Ye, C.; Li, H.; Jaroniec, M.; Qiao, S.-Z. Roadmap for Advanced Aqueous Batteries: From Design of Materials to Applications. *Sci. Adv.* **2020**, *6* (21), No. eaba4098.

(2) Wu, D.; Li, X.; Liu, X.; Yi, J.; Acevedo-Peña, P.; Reguera, E.; Zhu, K.; Bin, D.; Melzack, N.; Wills, R. G. A.; Huang, J.; Wang, X.; Lin, X.; Yu, D.; Ma, J. Roadmap on Aqueous Batteries. *J. Phys.: Energy* **2022**, *4*, 041501.

(3) Masquelier, C.; Croguennec, L. Polyanionic (phosphates, Silicates, Sulfates) Frameworks as Electrode Materials for Rechargeable Li (or Na) Batteries. *Chem. Rev.* **2013**, *113* (8), 6552−6591.

(4) Chen, S.; Wu, C.; Shen, L.; Zhu, C.; Huang, Y.; Xi, K.; Maier, J.; Yu, Y. Challenges and Perspectives for NASICON-Type Electrode Materials for Advanced Sodium-Ion Batteries. *Adv. Mater.* **2017**, *29* (48), 1700431.

(5) Singh, B.; Wang, Z.; Park, S.; Gautam, G. S.; Chotard, J.-N.; Croguennec, L.; Carlier, D.; Cheetham, A. K.; Masquelier, C.; Canepa, P. A. Chemical Map of NaSICON Electrode Materials for Sodium-Ion Batteries. *J. Mater. Chem. A* **2021**, *9* (1), 281−292.

(6) Mohamed, A. I.; Whitacre, J. F. Capacity Fade of NaTi2(PO4)3 in Aqueous Electrolyte Solutions: Relating pH Increases to Long Term Stability. *Electrochim. Acta* **2017**, *235*, 730−739.

(7) Pilipavičius, J.; Traškina, N.; Juodkazytė, J.; Vilčiauskas, L. The Mechanism of NaTi2(PO4)3 Aqueous Electrochemical Degradation Revisited. *Electrochim. Acta* **2023**, *465*, 142993.

(8) Tediashvili, D.; Pilipavičius, J.; Juodkazytė, J.; Vilčiauskas, L. On the Degradation of Vanadium-Based Phosphate Framework Electrode Materials in Aqueous Environments. *J. Electrochem. Soc.* **2023**, *170* (12), 120529.

(9) Petrulevičienė, M.; Pilipavičius, J.; Juodkazytė, J.; Gryaznov, D.; Vilčiauskas, L. Electrochemical Performance of NASICON-Structured Na3-x V2-xTix(PO4)3 ($0.0 < x < 1.0$) as Aqueous Na-Ion Battery Positive Electrodes. *Electrochim. Acta* **2022**, *424*, 140580.

(10) Saravanan, K.; Mason, C. W.; Rudola, A.; Wong, K. H.; Balaya, P. The First Report on Excellent Cycling Stability and Superior Rate Capability of Na3V2(PO4)3 for Sodium Ion Batteries. *Adv. Energy Mater.* **2013**, *3* (4), 444−450.

(11) Jian, Z.; Han, W.; Lu, X.; Yang, H.; Hu, Y.-S.; Zhou, J.; Zhou, Z.; Li, J.; Chen, W.; Chen, D.; Chen, L. Superior Electrochemical Performance and Storage Mechanism of Na3V2(PO4)3Cathode for Room-Temperature Sodium-Ion Batteries. *Adv. Energy Mater.* **2013**, *3* (2), 156−160.

(12) Chotard, J.-N.; Rousse, G.; David, R.; Mentré, O.; Courty, M.; Masquelier, C. Discovery of a Sodium-Ordered Form of Na3V2-(PO4)3 below Ambient Temperature. *Chem. Mater.* **2015**, *27* (17), 5982−5987.

(13) Park, S.; Wang, Z.; Choudhary, K.; Chotard, J.-N.; Carlier, D.; Fauth, F.; Canepa, P.; Croguennec, L.; Masquelier, C. Obtaining V2(PO4)3 by Sodium Extraction from Single-Phase NaxV2(PO4)3 ($1 < x < 3$) Positive Electrode Materials. *Nat. Mater.* **2025**, *24* (2), 234−242.

(14) Zhang, H.; Tan, X.; Li, H.; Passerini, S.; Huang, W. Assessment and Progress of Polyanionic Cathodes in Aqueous Sodium Batteries. *Energy Environ. Sci.* **2021**, *14* (11), 5788−5800.

(15) Yue, J.; Lin, L.; Jiang, L.; Zhang, Q.; Tong, Y.; Suo, L.; Hu, Y.-S.; Li, H.; Huang, X.; Chen, L. Interface Concentrated-confinement Suppressing Cathode Dissolution in Water-in-salt Electrolyte. *Adv. Energy Mater.* **2020**, *10* (36), 2000665.

(16) Yang, W.; Wang, X.; Lu, S.; Gao, Y.; Gao, T.; Guo, T.; Xie, Q.; Ruan, Y. Bimetallic Synergies Help the Application of Sodium Vanadyl Phosphate in Aqueous Sodium-Ion Batteries. *ChemSusChem* **2023**, *16* (8), No. e202202257.

(17) Jin, T.; Ji, X.; Wang, P.-F.; Zhu, K.; Zhang, J.; Cao, L.; Chen, L.; Cui, C.; Deng, T.; Liu, S.; Piao, N.; Liu, Y.; Shen, C.; Xie, K.; Jiao, L.; Wang, C. High-Energy Aqueous Sodium-Ion Batteries. *Angew. Chem. Int. Ed.* **2021**, *60* (21), 11943−11948.

(18) Gilankar, A.; Mitra, A.; Singh, J.; Das, S.; Majumder, S. B. Investigations on Different Strategies towards Improving the Electrochemical Properties of Na2VTi (PO4)3 for Symmetrical Sodium-Ion Batteries. *J. Alloys Compd.* **2021**, *851*, 156813.

(19) Shen, L.; Yang, H.; Jiang, Y.; Ma, J.; Sun, T.; Zhang, M.; Zhu, N. NASICON-Structured Na2VTi(PO4)3@C for Symmetric Aqueous Rechargeable Na-Ion Batteries with Long Lifespan. *ACS Sustain. Chem. Eng.* **2021**, *9* (9), 3490−3497.

(20) Zhang, B.; Zeng, T.; Liu, Y.; Zhang, J.-F. Effect of Ti-Doping on the Electrochemical Performance of Sodium Vanadium(III) Phosphate. *RSC Adv.* **2018**, *8* (10), 5523−5531.

(21) Huemer, B.; Jodlbauer, A.; Wilkening, M.; Krenn, H.; Knoll, P.; Würschum, R.; Hanzu, I.; Topolovec, S. *Operando* Monitoring the Redox Activity of Sodium Vanadium Titanium Phosphate Electrodes in Organic and Aqueous Electrolytes by Magnetometry. *J. Mater. Chem. A* **2025**, *13* (4), 2934−2942.
(22) Huang, Y.; Li, X.; Wang, J.; Miao, L.; Li, C.; Han, J.; Huang, Y. Superior Na-Ion Storage Achieved by Ti Substitution in Na3V2-(PO4)3. *Energy Storage Mater.* **2018**, *15*, 108−115.
(23) Wang, D.; Bie, X.; Fu, Q.; Dixon, D.; Bramnik, N.; Hu, Y.-S.; Fauth, F.; Wei, Y.; Ehrenberg, H.; Chen, G.; Du, F. Sodium Vanadium Titanium Phosphate Electrode for Symmetric Sodium-Ion Batteries with High Power and Long Lifespan. *Nat. Commun.* **2017**, *8* (1), 15888.
(24) Nakamoto, K.; Sakamoto, R.; Nishimura, Y.; Xia, J.; Ito, M.; Okada, S. A Trifluoroacetate-Based Concentrated Electrolyte for Symmetrical Aqueous Sodium-Ion Battery with NASICON-Type Na2VTi(PO4)3 Electrodes. *Electrochemistry (Tokyo)* **2021**, *89* (5), 415−419.
(25) Petrulevičienė, M.; Traškina, N.; Pilipavičius, J.; Juodkazytė, J.; Vilčiauskas, L. The Use of Reductive Agents for Developing Capacity Balanced Aqueous Sodium-ion Batteries. *Batter. Supercaps* **2023**, *6* (7), No. e202300129.
(26) Grey, C. P.; Dupré, N. NMR Studies of Cathode Materials for Lithium-Ion Rechargeable Batteries. *Chem. Rev.* **2004**, *104* (10), 4493−4512.
(27) Blanc, F.; Leskes, M.; Grey, C. P. In Situ Solid-State NMR Spectroscopy of Electrochemical Cells: Batteries, Supercapacitors, and Fuel Cells. *Acc. Chem. Res.* **2013**, *46* (9), 1952−1963.
(28) Pecher, O.; Carretero-González, J.; Griffith, K. J.; Grey, C. P. Materials' Methods: NMR in Battery Research. *Chem. Mater.* **2017**, *29* (1), 213−242.
(29) Zhang, E.; Wu, Y.-C.; Shao, H.; Klimavicius, V.; Zhang, H.; Taberna, P.-L.; Grothe, J.; Buntkowsky, G.; Xu, F.; Simon, P.; Kaskel, S. Unraveling the Capacitive Charge Storage Mechanism of Nitrogen-Doped Porous Carbons by EQCM and ssNMR. *J. Am. Chem. Soc.* **2022**, *144* (31), 14217−14225.
(30) Gonzalez-Correa, E.; Mazumder, M.; Kumar, K.; Ghosh, S.; Senguttuvan, P.; Clément, R. J. High Voltage Irreversibilities in NASICON Na3+*y*V2−*y*mg*y*(PO4)3 Cathodes. *Chem. Mater.* **2025**, *37* (16), 6323−6334.
(31) Broux, T.; Bamine, T.; Fauth, F.; Simonelli, L.; Olszewski, W.; Marini, C.; Ménétrier, M.; Carlier, D.; Masquelier, C.; Croguennec, L. Strong Impact of the Oxygen Content in Na3V2(PO4)2F3−*y*O*y* ($0 \leq y \leq 0.5$) on Its Structural and Electrochemical Properties. *Chem. Mater.* **2016**, *28* (21), 7683−7692.
(32) Liu, Z.; Hu, Y.-Y.; Dunstan, M. T.; Huo, H.; Hao, X.; Zou, H.; Zhong, G.; Yang, Y.; Grey, C. P. Local Structure and Dynamics in the Na Ion Battery Positive Electrode Material Na3V2(PO4)2F3. *Chem. Mater.* **2014**, *26* (8), 2513−2521.
(33) Klimavičius, V.; Traškina, N.; Dubauskas, A.; Manionis, M.; Pilipavičius, J.; Vilčiauskas, L. Multinuclear Solid-State NMR Study of the Aqueous Solid-Electrolyte Interphase Formation in NaTi2(PO4)-3. *ACS Appl. Energy Mater.* **2024**, *7* (24), 11665−11669.
(34) Allen, J. P.; Grey, C. P. Solution NMR of Battery Electrolytes: Assessing and Mitigating Spectral Broadening Caused by Transition Metal Dissolution. *J. Phys. Chem. C* **2023**, *127* (9), 4425−4438.
(35) Miliante, C. M.; Sanders, K. J.; McGoldrick, L. J.; Seriani, N.; Adams, B. D.; Goward, G. R.; Higgins, D.; Rubel, O. Unveiling the Origin of the Capacity Fade in MnO2 Zinc-Ion Battery Cathodes through an Analysis of the Mn Vacancy Formation. *arXiv* **2026**, arXiv:2602.13116.
(36) Leifer, N.; Aurbach, D.; Greenbaum, S. G. NMR Studies of Lithium and Sodium Battery Electrolytes. *Prog. Nucl. Magn. Reson. Spectrosc.* **2024**, *142*−*143*, 1−54.
(37) Zhou, L.; Leskes, M.; Ilott, A. J.; Trease, N. M.; Grey, C. P. Paramagnetic Electrodes and Bulk Magnetic Susceptibility Effects in the in Situ NMR Studies of Batteries: Application to Li1.08Mn1.92O4 Spinels. *J. Magn. Reson.* **2013**, *234*, 44−57.
(38) Pell, A. J.; Pintacuda, G.; Grey, C. P. Paramagnetic NMR in Solution and the Solid State. *Prog. Nucl. Magn. Reson. Spectrosc.* **2019**, *111*, 1−271.
(39) Zhang, Y.; Castets, A.; Carlier, D.; Ménétrier, M.; Boucher, F. Simulation of NMR Fermi Contact Shifts for Lithium Battery Materials: The Need for an Efficient Hybrid Functional Approach. *J. Phys. Chem. C* **2012**, *116* (33), 17393−17402.
(40) Britto, S.; Leskes, M.; Hua, X.; Hébert, C.-A.; Shin, H. S.; Clarke, S.; Borkiewicz, O.; Chapman, K. W.; Seshadri, R.; Cho, J.; Grey, C. P. Multiple Redox Modes in the Reversible Lithiation of High-Capacity, Peierls-Distorted Vanadium Sulfide. *J. Am. Chem. Soc.* **2015**, *137* (26), 8499−8508.
(41) Toby, B. H.; Von Dreele, R. B. GSAS-II: the genesis of a modern open-source all purpose crystallography software package. *J. Appl. Crystallogr.* **2013**, *46*, 544−549.
(42) Povar, I.; Spinu, O.; Zinicovscaia, I.; Pintilie, B.; Ubaldini, S. Revised Pourbaix Diagrams for the Vanadium − Water System. *J. Electrochem. Sci. Eng.* **2019**, *9* (2), 75−84.
(43) Baruah, B.; Roden, J. M.; Sedgwick, M.; Correa, N. M.; Crans, D. C.; Levinger, N. E. When Is Water Not Water? Exploring Water Confined in Large Reverse Micelles Using a Highly Charged Inorganic Molecular Probe. *J. Am. Chem. Soc.* **2006**, *128* (39), 12758−12765.
(44) Gee, B. A.; Wong, A. Vanadium-51 MAS and Static NMR Studies of the Binary V2O5−WO3 System. *J. Phys. Chem. B* **2003**, *107* (33), 8382−8387.
(45) Zhu, J.; Huang, Y. Solid-State 51V NMR Investigation of the Intercalation of Alkylamines into Layered Alpha-Vanadyl Phosphate. *Langmuir* **2010**, *26* (12), 10115−10121.
(46) Shi, C.; Muhtar, D.; Pei, Y.; Lu, X.; Liu, F.; Wang, D.; Lu, X.; Sun, Z. Suppressing V/Na Anti-Site Defects via Fluorine Doping Enables High-Voltage and Stable V-Based NASICON Cathodes for Sodium-Ion Batteries. *Adv. Energy Mater.* **2026**, *16* (21), No. e70898.
(47) Liu, R.; Zheng, S.; Yuan, Y.; Yu, P.; Liang, Z.; Zhao, W.; Shahbazian-Yassar, R.; Ding, J.; Lu, J.; Yang, Y. Counter-Intuitive Structural Instability Aroused by Transition Metal Migration in Polyanionic Sodium Ion Host. *Adv. Energy Mater.* **2021**, *11*, 2003256.
(48) Qiu, Q.; Li, C.; Liu, H.; Liao, Y.; Zhao, C.; Geng, F.; Shen, M.; Li, J.; Tong, W.; Hu, B. NMR Evidence for the Multielectron Reaction Mechanism of Na3V2(PO4)3 Cathode and the Impact of Polyanion Site Substitution. *J. Phys. Chem. C* **2021**, *125* (28), 15200−15209.
(49) Guiot, F.; Praud, C.; Quillard, S.; Humbert, B.; Ropers, M.-H.; Paris, M.; Terrisse, H. Surface reactivity of anatase particles towards phosphated species. *Colloids Surf., A* **2022**, *655*, 130232.
(50) Li, Y. J.; Whittingham, M. S. Hydrothermal Synthesis of New Metastable Phases: Preparation and Intercalation of a New Layered Titanium Phosphate. *Solid State Ionics* **1993**, *63*−*65*, 391−395.
(51) Rusanova-Naydenova, D.; Trublet, M.; Klysubun, W.; Cholsuk, C.; Iuga, D.; Dupree, R.; Antzutkin, O. N.; Persson, I. Synthesis and Structural Characterisation of Solid titanium(IV) Phosphate Materials by Means of X-Ray Absorption and NMR Spectroscopy. *Dalton Trans.* **2022**, *51* (21), 8192−8207.
(52) Tricot, G.; Montagne, L.; Delevoye, L.; Palavit, G.; Kostoj, V. Redox and structure of sodium-vanadophosphate glasses. *J. Non-Cryst. Solids* **2004**, *345*−*346*, 56−60.
(53) Montina, T.; Wormald, P.; Hazendonk, P. 13C Solid-State NMR of the Mobile Phase of Poly(vinylidene Fluoride). *Macromolecules* **2012**, *45* (15), 6002−6007.
(54) Darmstadt, H.; Roy, C.; Kaliaguine, S.; Xu, G.; Auger, M.; Tuel, A.; Ramaswamy, V. Solid State 13C-NMR Spectroscopy and XRD Studies of Commercial and Pyrolytic Carbon Blacks. *Carbon N. Y.* **2000**, *38* (9), 1279−1287.
(55) Peach, A.; Fabregue, N.; Erre, C.; Métro, T.-X.; Gajan, D.; Mentink-Vigier, F.; Scott, F.; Trébosc, J.; Voron, F.; Patris, N.; Gervais, C.; Laurencin, D. Capturing and Labeling CO2 in a Jar: Mechanochemical 17O-Enrichment and ssNMR Study of Sodium and Potassium (bi)carbonate Salts. *Chem. Sci.* **2025**, *16* (24), 10731−10741.